

NON-HERMITIAN TOPOLOGICAL ELECTRIC CIRCUITS WITH PROJECTIVE SYMMETRY

Wenjie Zhang¹, Yuting Yang^{1,2,*}, Xiaopeng Shen¹, Liwei Shi¹, Zhi Hong Hang^{3,4}

¹School of Materials and Physics, China University of Mining and Technology Xuzhou 221116, China

²State Key Laboratory of Millimeter Waves, Southeast University, Nanjing 210096, China

³School of Physical Science and Technology & Collaborative Innovation Center of Suzhou Nano Science and Technology, Soochow University, Suzhou 215006, China

⁴Institute for Advanced Study, Soochow University, Suzhou 215006, China

* Corresponding author: yangyt@cumt.edu.cn

ABSTRACT

Non-Hermitian topological insulators have attracted considerable attention due to their distinctive energy band characteristics and promising applications. Here, we systematically investigate non-Hermitian Möbius insulators and graphene-like topological semimetals from the projected symmetry and realize their corresponding topological phenomena in an electric circuit-based framework. By introducing a nonreciprocal hopping term consisting of negative impedance converters into a two-dimensional electric circuit, we establish an experimental platform that effectively demonstrates that introducing non-Hermitian terms significantly enhances the energy localization of topological edge states, which originate from the non-Hermitian skin effect. Furthermore, a thorough comparison of experimental measurements with numerical simulations validates the robustness and reliability of our electric circuit structure. This work not only reveals the physical properties of non-Hermitian topological materials but also provides valuable theoretical and experimental guidance for the implementation of topological circuits and the design of radiofrequency devices in the future.

1 Introduction

The symmetry-protected topological phases have been a hot topic in condensed matter physics and artificial periodic systems, such as acoustic and photonic crystals, and electric circuits [1, 2, 3, 4, 5, 6, 7, 8, 9]. The topological insulators have gathered significant attention due to their topologically protected edge states, which exhibit remarkable robustness against external disturbances and impurities. Various symmetries, such as the time-reversal symmetry and the point group symmetry, dictate the topological classification and topological band characterization. The recent studies have found that crystal symmetries are projectively represented under a \mathbb{Z}_2 gauge field (0 and π flux over the lattice), which impacts the algebra of spatial symmetry operations [10, 11, 12]. The artificial periodic systems with the time-reversal symmetry have intrinsic synthetic gauge field, which means the hopping amplitudes are real numbers that can take either positive or negative signs [13, 14]. The synthetic gauge field enriched the classification of topological phases. The broken primitive translational symmetries give rise to novel Möbius topological insulators with twisted edge bands and graphene-like semimetal phases with flat bands, which have been realized in acoustic crystals, photonic microring lattices, photonic waveguides and electric circuits [15, 16, 17, 18, 19, 20].

In a genuine open physical system, non-negligible interactions with the environment lead to a non-Hermitian Hamiltonian, including complex eigenvalues. The interplay between non-Hermitian and topological phases has induced many intriguing phenomena. A recent discovery is the breakdown of the conventional bulk-boundary correspondence, derived from non-Hermitian skin effects, where all eigenstates are localized near the edge of an open system [21, 22, 23, 24, 25]. Non-Hermitian skin effects have been investigated in meta-crystals and quantum walks [26, 27, 28, 29, 30, 31]. A non-Hermitian term can be conveniently introduced into an electric circuit [32, 33, 34, 35, 36], for example, by utilizing a negative-impedance converter with unidirectional current flow to create nonreciprocal hoppings [37, 38, 39]. With the help of the excellent boundary sensitivity of non-Hermitian skin effects and flexible construction of electric circuits,

it holds the significant potential for designing advanced topological radiofrequency devices, such as a sensor with high sensitivity [40, 41, 42].

Topological insulators with projected symmetry have been extensively investigated in many studies; however, the experimental demonstration for their non-Hermitian properties have not been performed. In this work, we construct non-Hermitian Möbius topological insulators and graphene-like semimetal phases within a two-dimensional electrical circuit. Nonreciprocal hopping is achieved through the use of negative-impedance converters. Both simulations and experimental results confirm the presence of the non-Hermitian skin effect.

2 Non-Hermitian Möbius insulator

We firstly consider a two-dimensional rectangular lattice model with π gauge flux per plaquette, proposed in Ref. [11, 13]. When the primitive translational symmetries along the x - and y - directions are preserved, fourfold degenerated Dirac points emerge at the corner of the first Brillouin zone. Breaking the primitive translational symmetry only along y -direction through staggered dimerization, the degenerated Dirac points are lifted, resulting in a band gap. The detailed projective symmetry is shown in Supplementary Material. This leads to the proposal of the Möbius insulator, characterized by a twisted edge band dispersion analogous to a Möbius strip. As illustrated in Fig. 1(a), the non-Hermitian Möbius insulator is constructed by introducing nonreciprocal hoppings. The parameter t represents the hopping along the y direction, while J_1 and J_2 denote the intra- and inter- coupling coefficients, respectively. The nonreciprocal and dimerized hoppings are $J_{1\pm} = J_1 \pm \delta_x$ and $J_{2\pm} = J_2 \pm \delta_x$ along the x direction. The Hamiltonian of this tight-binding model is [43]:

$$H = \begin{bmatrix} 0 & T_y & V + \Delta_x & 0 \\ T_y & 0 & 0 & -(V + \Delta_x) \\ V^* + \Delta_x & 0 & 0 & T_y \\ 0 & -(V^* + \Delta_x) & T_y & 0 \end{bmatrix} \quad (1)$$

where $T_y = 2t \cos(k_y/2)$, $V = -J_1 e^{ik_x/2} - J_2 e^{-ik_x/2}$, and $\Delta_x = -2i\delta_x \sin(k_x/2)$.

The electric circuit realization of the non-Hermitian Möbius insulator is shown in the right panel in Fig. 1(a). The hopping parameter t corresponds to the capacitance value C_1 between two nodes in the designed circuit configuration. The positive hoppings J_1 and J_2 correspond to capacitance values C_1 and C_2 , respectively, while the negative hoppings correspond to inductance values L_1 and L_2 . The nonreciprocal term δ_x is achieved via a negative impedance converter with a current inversion (INIC), which incorporates an operational amplifier along with a resistor (denoted as R_a) and a capacitor (denoted as C_2). This configuration is characterized by a positive capacitance C_g in one direction and a negative capacitance $-C_g$ in the reverse direction. We can obtain the Laplace form of its nodal voltage equation:

$$\begin{pmatrix} I_1 \\ I_2 \end{pmatrix} = i\omega C_g \begin{pmatrix} -1 & 1 \\ -1 & 1 \end{pmatrix} \begin{pmatrix} V_1 \\ V_2 \end{pmatrix} \quad (2)$$

The parameters in the lattice model are set as $t_1 = J_1 = 1$ and $J_2 = 3.3$. When the hopping ratio $J_2/J_1 = C_2/C_1 = L_1/L_2$ is greater than 1, the system is a topological Möbius insulator [15]. Consequently, the values of circuit components are selected as $C_1 = 10$ nF, $C_2 = 33$ nF, $L_1 = 10$ μ H, and $L_2 = 3.3$ μ H. The inductance values L_2 should be 3.03 μ H. To simplify the selection of circuit components for the experimental setup, L_2 is chosen to be 3.3 μ H. Owing to the robustness of the topological insulator, the slight change does not affect the circuit characteristics. Nodes 1 and 3 should be connected in parallel to a ground capacitor C_3 (43 nF), while nodes 2 and 4 are connected in parallel to a ground inductor L_3 (2.5 μ H). The non-Hermitian parameter δ is defined as the ratio of the capacitance C_g to C_1 , i.e., $\delta = C_g/C_1$, where the capacitance C_g varies under the fixed C_1 . This ratio characterizes the nonreciprocal hopping strength in the system and plays a critical role in the manifestation of the non-Hermitian skin effect.

According to the Kirchhoff current law and Bloch theorem, we can obtain the circuit conductance matrix (detailed derivation in Sec. 1 within Supplementary Material):

$$J_m = i\omega C_m + \frac{L_m}{i\omega} \quad (3)$$

where

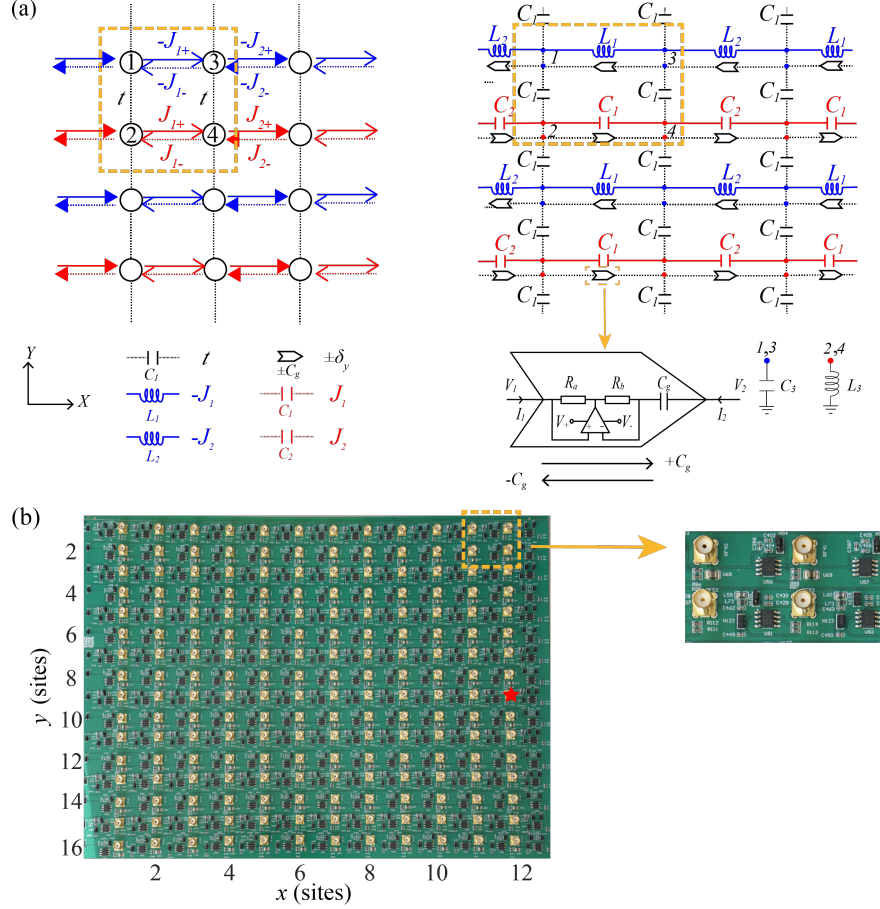


Figure 1: (a) Left panel: Schematic of the tight-binding model of the non-Hermitian Möbius insulator, realized by adding nonreciprocal hoppings. Right panel: Electric circuit realization of the non-Hermitian Möbius insulator through introducing negative-impedance converters. A unit cell indicated by a rectangular box includes four nodes labeled with the numbers. (b) Photograph of the electric circuit board in the experimental measurement.

$$C_m = \begin{bmatrix} t_1 & A_y & \sigma & 0 \\ A_y & t_2 & 0 & B_x - \sigma \\ \sigma & 0 & t_1 & A_y \\ 0 & B_x^* - \sigma & A_y & t_2 \end{bmatrix} \quad (4)$$

with $t_1 = 2C_1 + C_3$, $t_2 = 3C_1 + C_2$, $A_y = -2C_1 \cos(k_y/2)$, $B_x = -C_1 e^{ik_x/2} - C_2 e^{-ik_x/2}$, and $\sigma = 2iC_g \sin(k_x/2)$,

$$L_m = \begin{pmatrix} \frac{1}{L_1} + \frac{1}{L_2} & 0 & -\frac{e^{ik_x/2}}{L_1} - \frac{e^{-ik_x/2}}{L_2} & 0 \\ 0 & \frac{1}{L_3} & 0 & 0 \\ -\frac{e^{-ik_x/2}}{L_1} - \frac{e^{ik_x/2}}{L_2} & 0 & \frac{1}{L_1} + \frac{1}{L_2} & 0 \\ 0 & 0 & 0 & \frac{1}{L_3} \end{pmatrix} \quad (5)$$

To solve for the eigenfrequency of the circuit system, we can let $I_n = 0$, and get $JV = 0$. I is the current and V is the node voltage. We can obtain the eigenfrequency of the non-Hermitian circuit system by solving $\det[J] = 0$. This method has some limitations. When the derivative matrix is complex, it is difficult to find the eigenfrequency. By taking the derivative of V for $JV = 0$ with respect to time, we can get the following two differential equations [34]:

$$-i \frac{d}{dt} \dot{V} = i \frac{L}{C} V \quad (6)$$

$$-i \frac{d}{dt} V = -i E \dot{V} \quad (7)$$

where E is the unit matrix. The first-order derivative in the time domain is equivalent to multiplying by $i\omega$ in the frequency domain. Hence, we can derive the relationship and obtain:

$$-i \cdot i\omega \begin{bmatrix} \dot{V} \\ V \end{bmatrix} = i \begin{bmatrix} 0 & \frac{L}{C} \\ -E & 0 \end{bmatrix} \begin{bmatrix} \dot{V} \\ V \end{bmatrix} \quad (8)$$

This formula exhibits a formal similarity to the Schrödinger equation, allowing us to make the Hamiltonian matrix equal to:

$$H = \begin{bmatrix} 0 & \frac{L}{C} \\ -E & 0 \end{bmatrix} \quad (9)$$

The eigenvalues of the $H(k)$ matrix directly correspond to the angular frequencies of the system. The eigenvalues obtained through the solution of $\det(H)$ are divided into two distinct parts (ω, ω^*). The real part of ω is positive and can be utilized as the eigenfrequency of the circuit.

The non-Hermitian skin effect is induced through tuning the nonreciprocal terms in the electric circuit. By calculating the eigenvalues, the theoretical dispersion curves can be obtained under the periodic boundary condition (PBC) and open boundary condition (OBC). The eigenfrequencies under the PBC along x and y directions (denoted as x/y-PBC) form closed loops in the complex plane for each fixed k_y , as shown in Fig. 2(a). The eigenvalues are plotted under x-OBC and y-PBC, indicated by black lines, which form open arcs corresponding to the non-Hermitian skin modes. The real eigenfrequency of the dispersion under x-OBC and y-PBC are displayed in Figs. 2(c) and 2(e), corresponding to the nonreciprocal hopping strength $\delta = 0.1$ and 1, respectively. Two twisted edge bands denoted by red lines emerge within the band gap, fully detached from the bulk bands. These real edge bands are similar with those in Hermitian Möbius insulator. When $\delta = 0.1$, the non-Hermitian skin effect is relatively weak, and the imaginary part of the eigenfrequency is very small. Under $\delta = 1$, the imaginary part of the frequency is large. The ratio δ varies as a function of frequencies (see Fig. S3 in Supplementary Material). The nonreciprocal term has a more pronounced impact on the system, leading to a notably enhanced non-Hermitian skin effect.

Subsequently, we construct a matrix consisting of eigenvectors, where each column contains information about all nodes at a specific frequency. We clarify that the eigenvector of the effective Hamiltonian is denoted as $\psi = \begin{bmatrix} V \\ \dot{V} \end{bmatrix}$, and we define $\varphi_i = |\psi_i|^2$ as the nodal modal intensity. We extract the eigenvectors of the edge frequency dispersions and perform a conjugate product operation on them to obtain the distribution of the eigenstates (see the detailed derivation in Supplementary Material), as shown in Figs. 3(a) and 3(b), corresponding to nonreciprocal hopping strength $\delta = 0.1$ and $\delta = 1$ respectively. We also extracted several sets of eigenvectors corresponding to the bulk bands at lower and higher frequencies indicated by blue and red lines respectively, as displayed in Figs. 3(c) and 3(d). It clearly shows that as the non-Hermitian coefficient increases, the energy of both the edge states and the bulk bands concentrate around the boundary of the electric circuit structure, induced by the non-Hermitian skin effect.

In order to deeply investigate the properties of the non-Hermitian skin effect in the Möbius topological insulator, we carry out the simulations and experiments in a two-dimensional electric circuit model containing 8×6 unit cells. In the experimental realization, we design and fabricate a printed circuit board (PCB) as shown in Fig. 1(b). The excited source is placed in the middle of the right boundary marked by a green star in Fig. 4. This configuration aims to enhance the response of the edge states and ensure the effective excitation of the topological modes propagating along the edge. By measuring the voltage response at each node of the electric circuit, we obtain voltage amplitude distributions in the experiments. When the nonreciprocal hopping strength $\delta = 0.1$, the simulated and experimental results at 486 kHz show that the voltage amplitude at the right boundary is very large compared with that in the bulk, demonstrating the existence of topological edge states, as displayed in Figs. 4(a) and 4(b). For the nonreciprocal strength $\delta = 1$, the edge state is significantly concentrated in the boundary region of the circuit induced by the non-Hermitian skin effect, as shown in Figs. 4(c) and 4(d). Figure 4(e) demonstrates the edge states exponentially decay perpendicular to the propagating direction for $\delta = 1$. The voltage amplitude decays rapidly from the right edge toward the left along x direction, indicating pronounced edge localization. Figure 4(f) illustrates the simulated and measured voltage amplitude at one edge node within the frequency range of 300 to 600 kHz corresponding to the twist edge bands. The experimentally observed frequency resonance peaks agree well with simulation results. We do not consider the resistance of the components in the simulated electric circuit, leading to very high resonance peaks. To well make

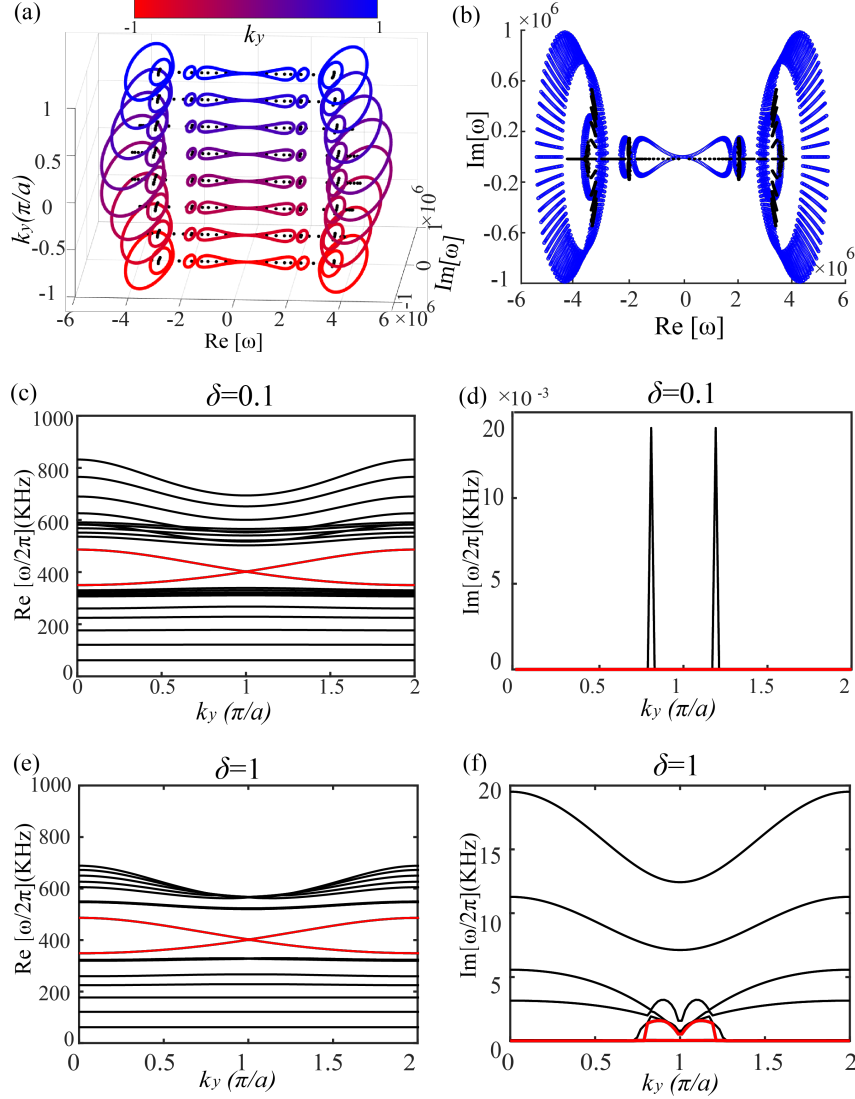


Figure 2: (a) Complex frequency spectra of the non-Hermitian Möbius insulator at different wave vector k_y for the nonreciprocal hopping strength $\delta = 1$. The frequency spectra with closed loops correspond to the electric circuit system under x-PBC and y-PBC, while the open arcs are plotted under x-OBC and y-PBC. (b) Projection of complex frequency spectra from panel (a). (c) and (e) Real part of eigenfrequencies with wave vector k_y for $\delta = 0.1$ and $\delta = 1$ respectively, while considering x-OBC and y-PBC within the non-Hermitian circuit system. The black curves represent the bulk bands, and the red curves indicate the twisted edge bands. (d) Imaginary part of eigenfrequencies for $\delta = 0.1$ and $\delta = 1$, respectively.

comparison between simulations and experiments, the voltage amplitudes are normalized individually based on their respective maximum values. A minor discrepancy is attributed to the non-ideal characteristics of components such as capacitors, inductors, and circuit wiring, leading to significant resistive losses during the experiment (see the detailed description in Supplementary Material). The operating characteristics of the operational amplifier are highly sensitive to peripheral circuits and are susceptible to a variety of experimental environmental factors such as power supply noise and poor grounding.

To quantify the degree of localization of the edge states, we define [44]

$$R_l = \frac{\int_{\Pi_s} |V|^2 dx dy}{\int_{\Pi} |V|^2 dx dy} \quad (10)$$

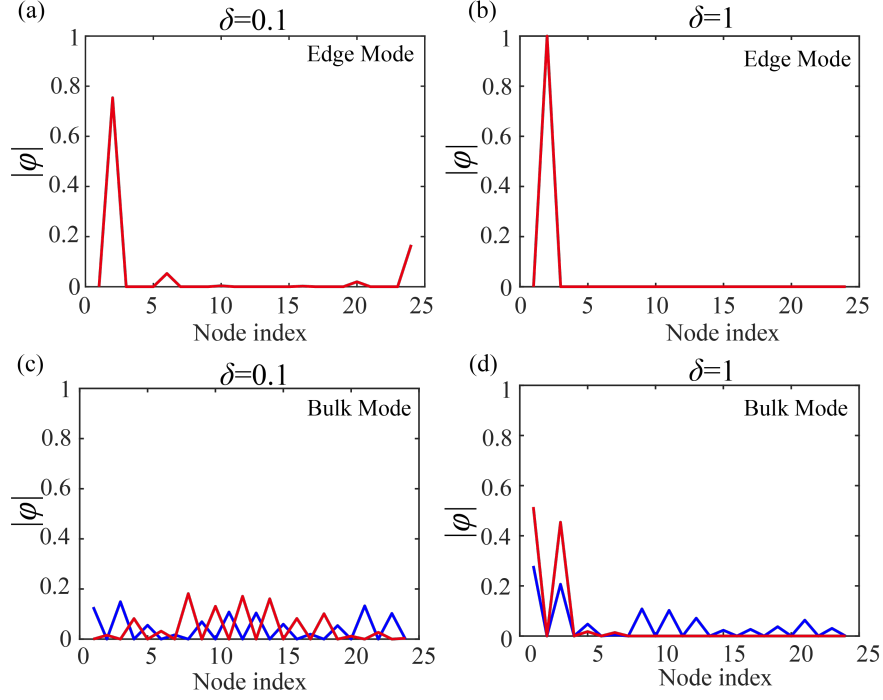


Figure 3: (a) and (b) Eigenstate distribution at the corresponding edge state frequencies in a non-Hermitian topological electric circuit when nonreciprocal hopping strength $\delta = 0.1$ and 1, respectively. (c) and (d) Bulk-state distribution corresponding to bulk band frequencies when $\delta = 0.1$ and 1.

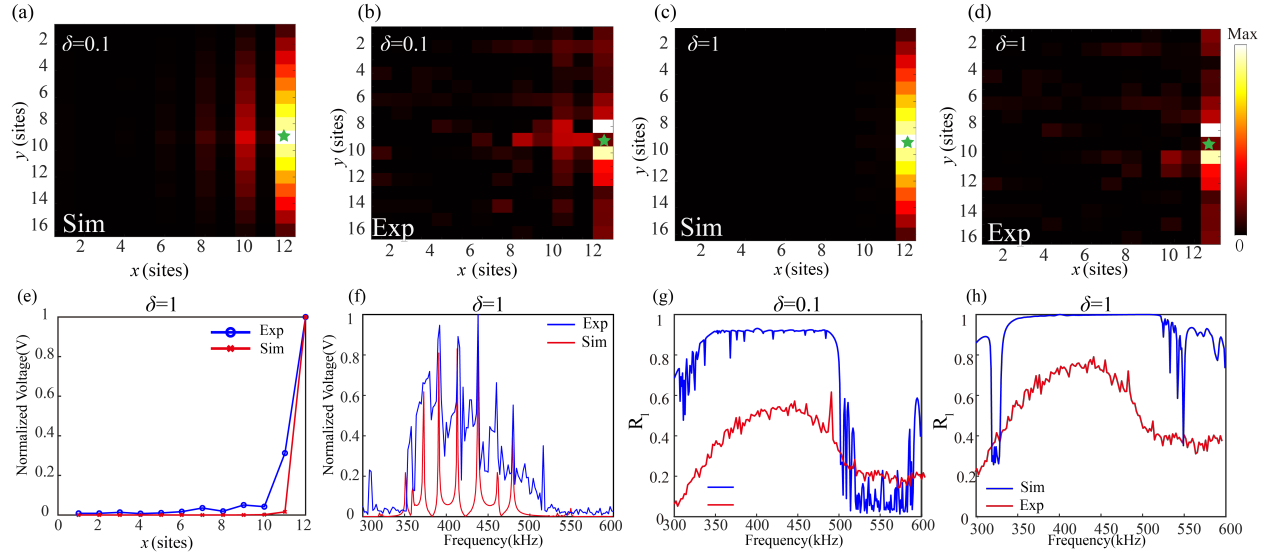


Figure 4: Simulated and experimental distribution of the voltage amplitude within the electric circuit at 486 kHz corresponding to the topological edge state at the nonreciprocal hopping strength $\delta = 0.1$ in (a)-(b) and $\delta = 1$ in (c)-(d), respectively. The localized edge states are induced by non-Hermitian skin effect. (e) Normalized voltage amplitude distribution along the x direction in (c) and (d). (f) Normalized voltage amplitude as a function of frequencies within 300-600 kHz. (g) and (h) Simulated and measured ratio R_l of edge-localized states.

where $|V|$ is the voltage amplitude, Π denotes the entire area of the electric circuit, and Π_s denotes the area covering the rightmost unit cells in the circuit structure. As illustrated in Figs. 4(g) and 4(h), the simulated ratio R_l approaches to 1

when the nonreciprocal hopping strength $\delta = 1$, demonstrating the strong boundary localization of the edge state within a broad frequency range. The experimentally measured R_l exhibits prominent peaks within the bandgap, and remains low at other frequencies. Both these observations confirm the edge state localization caused by the non-Hermitian skin effect.

3 Non-Hermitian graphene-like topological semimetals

As shown in Fig. 5, we design a rectangular lattice model with alternative dimerization. The primitive translation symmetries along x - and y - directions are both broken, which splits the fourfold Dirac point into two twofold nodal points [13]. By introducing the non-Hermitian hopping term based on this rectangular lattice, we construct a non-Hermitian graphene-like semimetal phase with flat bands. The corresponding circuit model is consistent with the construction method of the non-Hermitian Möbius insulator, utilizing capacitors and inductors combined with asymmetric hopping parameters to achieve non-Hermitian characteristics.

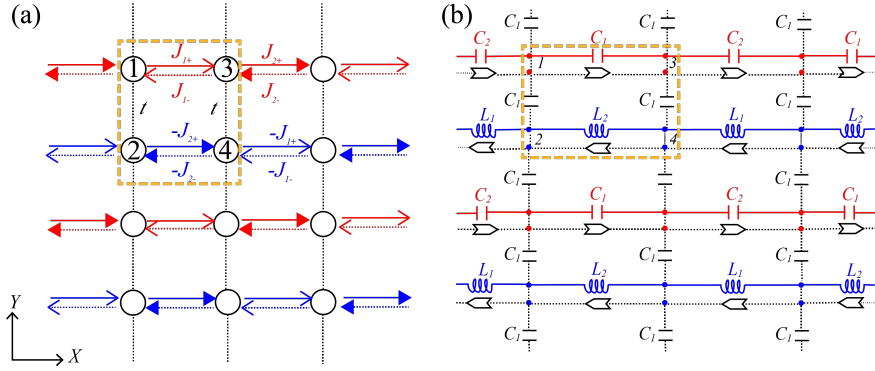


Figure 5: (a) and (b) Tight-binding model and its equivalent circuit model of a non-Hermitian graphene-like topological semimetal.

The admittance matrix of the non-Hermitian graphene-like semimetal phase is given as follows (detailed derivation in Sec. I within Supplementary Material):

$$J_p = i\omega C_p + \frac{1}{i\omega} L_p \quad (11)$$

where

$$C_p = \begin{bmatrix} t_2 & A_y & B_x - \sigma & 0 \\ A_y & t_1 & 0 & \sigma \\ B_x^* - \sigma & 0 & t_2 & A_y \\ 0 & \sigma & A_y & t_1 \end{bmatrix} \quad (12)$$

and

$$L_p = \begin{bmatrix} \frac{1}{L_3} & 0 & 0 & 0 \\ 0 & \frac{1}{L_1} + \frac{1}{L_2} & 0 & -\frac{1}{L_2} e^{ik_x/2} - \frac{1}{L_1} e^{-ik_x/2} \\ 0 & 0 & \frac{1}{L_3} & 0 \\ 0 & -\frac{1}{L_2} e^{-ik_x/2} - \frac{1}{L_1} e^{ik_x/2} & 0 & \frac{1}{L_1} + \frac{1}{L_2} \end{bmatrix} \quad (13)$$

By solving this eigen-equation, we obtain the band dispersion of the non-Hermitian electric circuit. A relatively flat band, denoted by red lines, emerges within the band gap of the graphene-like topological semimetal, as shown in Figs. 6(a) and 6(b). We investigate the relationship between the nonreciprocal hopping strength δ and the frequency spectrum. The result indicates that significant imaginary spectra appear when δ exceeds 0.15, increasing with larger values of δ , as displayed in Figs. 6(c) and 6(d). The stronger nonreciprocal hopping term leads to more pronounced non-Hermitian skin effect. Observations of the energy field distribution provide direct evidence for this non-Hermitian skin effect. As depicted in Figs. 6(e) and 6(f), as δ increases, the edge state energy becomes highly concentrated at the system boundaries, while the bulk state distribution rapidly decays. This phenomenon aligns with recent discussions on the generalized bulk-boundary correspondence [23] in non-Hermitian systems, further substantiating the non-Hermitian skin effect in graphene-like topological semimetals.

In the experimental design, we employ the same PCB previously utilized in our study of Möbius topological insulators. By flexibly adjusting jumper caps, various topological structures can be achieved without replacing the circuit board

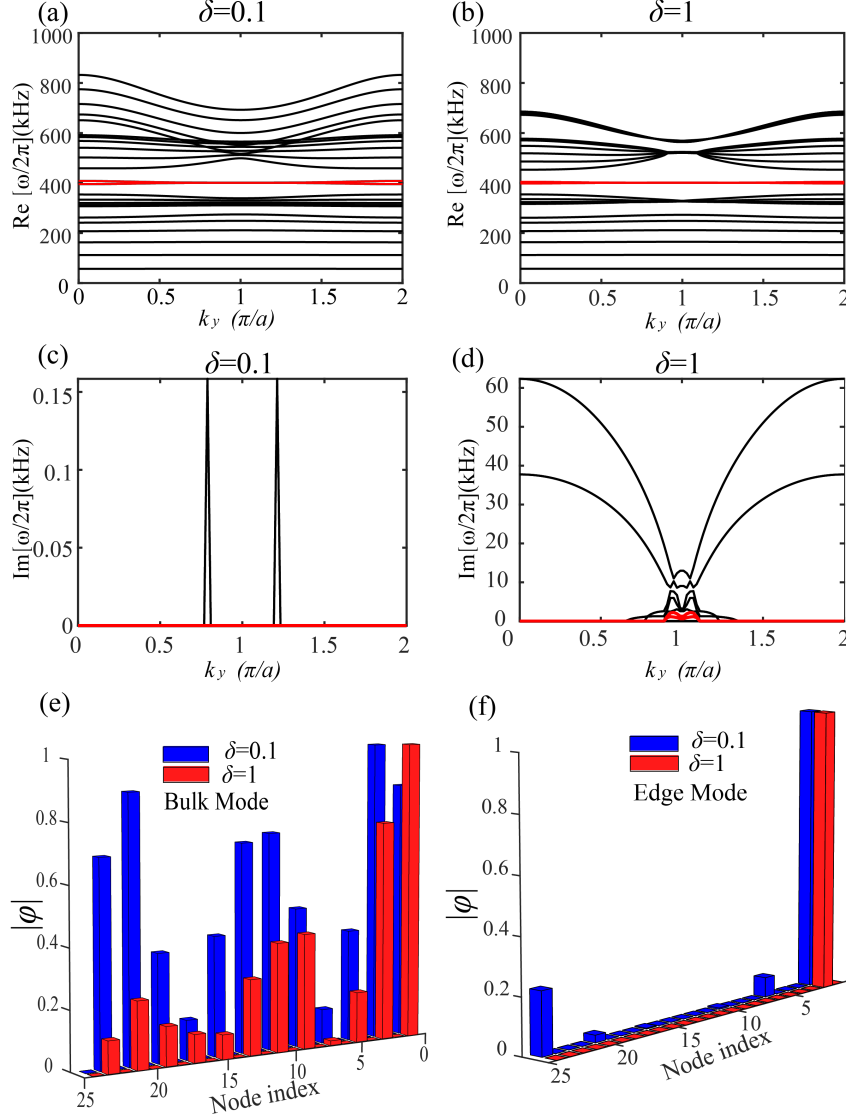


Figure 6: (a) and (b) Dispersion relation of the non-Hermitian graphene-like topological semimetal circuit. Real parts of the frequency are functioned as k_y for the nonreciprocal hopping strength $\delta = 0.1$ and $\delta = 1$ respectively. (c) and (d) Imaginary part of the frequency, showing enhanced non-Hermitian skin effect as δ increases. (e) and (f) Normalized energy distribution of bulk and edge states in the graphene-like topological semimetal structure for $\delta = 0.1$ and $\delta = 1$, respectively.

itself, thereby enabling precise control over periodic hopping parameters and asymmetric hopping terms. Additionally, the capacitance C_g can be rapidly replaced and adjusted through jumper caps, facilitating a systematic investigation of the impact of non-Hermitian parameters on the topological properties. Simulation results indicate that voltage amplitudes at the boundary are significantly higher than those in the bulk of the electric circuit at 400 kHz, corresponding to the edge state frequency, as shown in Fig. 7(a). This clearly demonstrates the significant concentration of topologically protected edge states at the boundary. In contrast, at 558 kHz corresponding to the bulk state frequency, the initial energy distribution spreads into the bulk, as shown in Fig. 7(c). However, with the introduction of non-Hermitian hopping terms, the energy rapidly redistributes towards the edges, exhibiting a pronounced non-Hermitian skin effect, as illustrated in Figs. 7(b) and 7(d). Notably, this skin effect is not limited to edge states but can be observed in bulk states. Figure 7(e) illustrates the simulated and experimentally measured normalized voltage amplitudes at one edge node as a function of frequencies. The highest voltage peak corresponds to the frequency of the flat edge state dispersion. Figure 7(f) displays the irregular normalized voltage peaks at one bulk node. With further increases in

the non-Hermitian parameter, the energy tends to accumulate more at the edges for both edge and bulk states. This phenomenon indicates that the non-Hermitian hopping term not only enhances the bulk-boundary correspondence of the system but also profoundly reshapes the spatial distribution of the overall energy field. These findings strongly confirm the universality of the non-Hermitian skin effect and its significant impact on the dynamical behavior of the system.

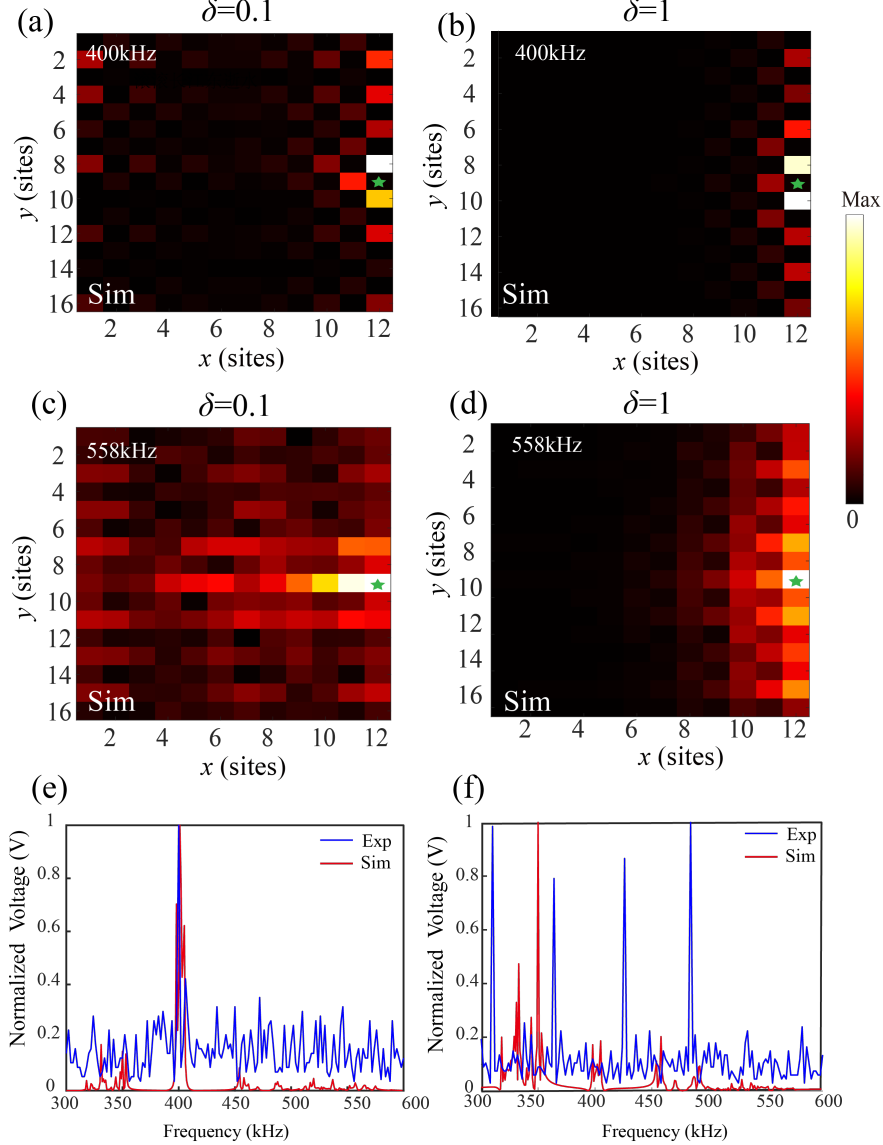


Figure 7: (a) and (b) Voltage amplitude distribution of edge states at 400 kHz in the graphene-like topological semimetal structure for the nonreciprocal hopping strength $\delta = 0.1$ and $\delta = 1$, respectively. (c) and (d) Voltage amplitude of bulk states at 558 kHz for $\delta = 0.1$ and $\delta = 1$, respectively. (e) Simulated and experimental normalized voltage amplitude at the edge node as a function of frequency within 300–600 kHz. (f) Simulated and measured normalized voltage amplitude at one bulk node as a function of frequency.

To better understand the non-Hermitian skin effect in our circuit models, we compare its mechanism and manifestation with those of representative non-Hermitian systems, including the Hatano-Nelson model [45, 46, 47] and the non-Hermitian Su-Schrieffer-Heeger (SSH) model with nonreciprocal hoppings [48, 49]. In these models, the non-Hermitian skin effect arises from asymmetric hopping amplitudes, leading to unidirectional mode localization and spectral winding in the complex plane. Our non-Hermitian Möbius circuit exhibits the non-Hermitian skin effect as a result of broken

translation symmetry, allowing us to study how twisted edge dispersions are deformed under nonreciprocal couplings. Meanwhile, in the non-Hermitian graphene-like semimetal, bulk states and edge states develop edge localization, especially near the flat-band region, revealing a bulk-band skin effect.

4 Conclusion

This study provides a systematic and in-depth investigation into the realization and characteristics of non-Hermitian Möbius insulators and graphene-like topological semimetals implemented within circuit-based platforms, incorporating theoretical modeling, numerical simulations and experimental verification. The results conclusively demonstrate that introducing nonreciprocal hopping mechanisms is a crucial condition for achieving non-Hermitian topological states. Moreover, the tuning of non-Hermitian parameters not only markedly enhances the energy localization of topological edge states and the intensity of the non-Hermitian skin effect, but also highlights the universality of such topological features within rectangular lattice configurations. These findings provide robust theoretical and experimental support for the design and optimization of non-Hermitian topological materials. More importantly, this work bridges the gap between Hamiltonian models of non-Hermitian topological phases and experimentally realizable circuit-based systems. Such an approach enables precise experimental validation of theoretical predictions and lays a solid foundation for extending these concepts to a broader array of applications, including photonic/acoustic topological devices and quantum simulation platforms. The electric circuit framework and analytical methods develop herein not only serve as a general paradigm for future systematic research and engineering optimization of non-Hermitian topological systems, but also chart a new course for the advancement of topological circuits and related emerging fields. Our study provides a platform to investigate the interplay between non-Hermiticity, topological band engineering, and boundary localization. Beyond its fundamental interest, the observed non-Hermitian skin effect and its controllability in electric circuits may also have practical implications. Given the recent successes of non-Hermitian circuit-based sensors with ultrahigh sensitivity [50, 51, 52], we believe that incorporating non-Hermitian skin effect and edge state dispersions of both Möbius-type and flat-band-type could offer new opportunities for designing robust and tunable sensing devices on both PCB and chip platforms.

Note added. – After submission, we became aware of Ref. [53], realizing the non-Hermitian acoustic Möbius insulator by introducing different loss materials, which differs for our proposed Non-Hermitian Möbius topological circuit work by introducing the nonreciprocal hopping term.

References

- [1] M. Z. Hasan and C. L. Kane. Colloquium: topological insulators. *Rev. Mod. Phys.*, 82(4):3045–3067, 2010.
- [2] A. B. Khanikaev, S. H. Mousavi, W. K. Tse, M. Kargarian, A. H. MacDonald, and G. Shvets. Photonic topological insulators. *Nat. Mater.*, 12(3):233–239, 2013.
- [3] L. Lu, J. D. Joannopoulos, and M. Soljačić. Topological photonics. *Nat. Photonics*, 8(11):821–829, 2014.
- [4] X. T. He, E. T. Liang, J. J. Yuan, H. Y. Qiu, X. D. Chen, F. L. Zhao, and J. W. Dong. A silicon-on-insulator slab for topological valley transport. *Nat. Commun.*, 10(1):872, 2019.
- [5] Z. J. Yang, F. Gao, X. Shi, X. Lin, Z. Gao, Y. Chong, and B. Zhang. Topological acoustics. *Phys. Rev. Lett.*, 114(11):114301, 2015.
- [6] J. Lu, C. Qiu, L. Ye, X. Fan, M. Ke, F. Zhang, and Z. Liu. Observation of topological valley transport of sound in sonic crystals. *Nat. Phys.*, 13(4):369–374, 2017.
- [7] N. Jia, C. Owens, A. Sommer, D. Schuster, and J. Simon. Time- and site-resolved dynamics in a topological circuit. *Phys. Rev. X*, 5(2):021031, 2015.
- [8] C. H. Lee, S. Imhof, C. Berger, F. Bayer, J. Brehm, L. W. Molenkamp, T. Kiessling, and R. Thomale. Topoelectrical circuits. *Commun. Phys.*, 1(1):1–9, 2018.
- [9] R. Yu, Y. X. Zhao, and A. P. Schnyder. 4d spinless topological insulator in a periodic electric circuit. *Nat. Sci. Rev.*, 7(8):1288–1295, 2020.
- [10] Y. X. Zhao, Y.-X. Huang, and S. A. Yang. Z₂-projective translational symmetry protected topological phases. *Phys. Rev. B*, 102(16):161117, 2020.
- [11] Y. X. Zhao, C. Chen, X.-L. Sheng, and S. A. Yang. Switching spinless and spinful topological phases with projective pt symmetry. *Phys. Rev. Lett.*, 126(19):196402, 2021.
- [12] L. B. Shao, Q. Liu, R. Xiao, S. A. Yang, and Y. Zhao. Gauge-field extended k-p method and novel topological phases. *Phys. Rev. Lett.*, 127(7):076401, 2021.

- [13] H. Xue, Z. Wang, Y. X. Huang, et al. Projectively enriched symmetry and topology in acoustic crystals. *Phys. Rev. Lett.*, 128(11):116802, 2022.
- [14] Y. Meng, S. Lin, B. Shi, et al. Spinful topological phases in acoustic crystals with projective pt symmetry. *Phys. Rev. Lett.*, 130(2):026101, 2023.
- [15] T. Li, J. Du, Q. Zhang, Y. Li, X. Fan, F. Zhang, and C. Qiu. Acoustic möbius insulators from projective symmetry. *Phys. Rev. Lett.*, 128(11):116803, 2022.
- [16] C. Jiang, Y. Song, X. Li, P. Lu, and S. Ke. Photonic möbius topological insulator from projective symmetry in multiorbital waveguides. *Opt. Lett.*, 48(9):2337–2340, 2023.
- [17] Z. Liu, G. Wei, H. Wu, and J. J. Xiao. Möbius edge band and weyl-like semimetal flat-band in topological photonic waveguide array by synthetic gauge flux. *Nanophotonics*, 12(17):3481–3490, 2023.
- [18] S. Bao, J. Chang, J. Wu, and Z. Xu. Circuit realization of möbius insulators. *Phys. Rev. A*, 108(1):013508, 2023.
- [19] Y. Liu, C. Jiang, W. Wen, Y. Song, X. Li, P. Lu, and S. Ke. Topological phases in photonic microring lattices with projective symmetry. *Phys. Rev. A*, 109(1):013516, 2024.
- [20] P. Lai, J. Wu, Z. Pu, Q. Zhou, J. Lu, H. Liu, W. Deng, H. Cheng, S. Chen, and Z. Liu. Real-projective-plane hybrid-order topological insulator realized in phononic crystals. *Phys. Rev. Appl.*, 21(4):044002, 2024.
- [21] Z. Gong, Y. Ashida, K. Kawabata, K. Takasan, S. Higashikawa, and M. Ueda. Topological phases of non-hermitian systems. *Phys. Rev. X*, 8(3):031079, 2018.
- [22] S. Yao, F. Song, and Z. Wang. Non-hermitian chern bands. *Phys. Rev. Lett.*, 121(3):136802, 2018.
- [23] S. Yao and Z. Wang. Edge states and topological invariants of non-hermitian systems. *Phys. Rev. Lett.*, 121(8):086803, 2018.
- [24] N. Okuma, K. Kawabata, K. Shiozaki, and M. Sato. Topological origin of non-hermitian skin effects. *Phys. Rev. Lett.*, 124(8):086801, 2020.
- [25] D. S. Borgnia, A. J. Kruchkov, and R.-J. Slager. Non-hermitian boundary modes and topology. *Phys. Rev. Lett.*, 124(5):056802, 2020.
- [26] R. El-Ganainy, K. G. Makris, M. Khajavikhan, Z. H. Musslimani, S. Rotter, and D. N. Christodoulides. Non-hermitian physics and pt symmetry. *Nat. Phys.*, 14(1):11–19, 2018.
- [27] Ş. K. Özdemir, S. Rotter, F. Nori, and L. Yang. Parity–time symmetry and exceptional points in photonics. *Nat. Mater.*, 18(8):783–798, 2019.
- [28] H. Gao, H. Xue, Z. Gu, T. Liu, J. Zhu, and B. Zhang. Non-hermitian route to higher-order topology in an acoustic crystal. *Nat. Commun.*, 12(1):1888, 2021.
- [29] Q. Zhang, Y. Li, H. Sun, X. Liu, L. Zhao, X. Feng, X. Fan, and C. Qiu. Observation of acoustic non-hermitian bloch braids and associated topological phase transitions. *Phys. Rev. Lett.*, 130(1):017201, 2023.
- [30] Q. Zhou, J. Wu, Z. Pu, J. Lu, X. Huang, W. Deng, M. Ke, and Z. Liu. Observation of geometry-dependent skin effect in non-hermitian phononic crystals with exceptional points. *Nat. Commun.*, 14(1):4569, 2023.
- [31] L. Xiao, X. Zhan, Z. H. Bian, K. K. Wang, X. Zhang, X. P. Wang, J. Li, K. Mochizuki, D. Kim, N. Kawakami, W. Yi, H. Obuse, B. C. Sanders, and P. Xue. Observation of topological edge states in parity-time-symmetric quantum walks. *Nat. Phys.*, 13(11):1117–1123, 2017.
- [32] Y. Choi, C. Hahn, J. W. Yoon, and S. H. Song. Observation of an anti-pt-symmetric exceptional point and energy-difference conserving dynamics in electrical circuit resonators. *Nat. Commun.*, 9(1):1–6, 2018.
- [33] S. Liu, S. Ma, C. Yang, L. Zhang, W. Gao, Y. J. Xiang, T. J. Cui, and S. Zhang. Gain- and loss-induced topological insulating phase in a non-hermitian electrical circuit. *Phys. Rev. Appl.*, 13(1):014047, 2020.
- [34] S. Liu, R. Shao, S. Ma, L. Zhang, O. You, H. Wu, Y. J. Xiang, T. J. Cui, and S. Zhang. Non-hermitian skin effect in a non-hermitian electrical circuit. *Research*, page 5608038, 2021.
- [35] J. Wu, X. Huang, Y. Yang, W. Deng, J. Lu, W. Deng, and Z. Liu. Non-hermitian second-order topology induced by resistances in electric circuits. *Phys. Rev. B*, 105(19):195127, 2022.
- [36] T. Hofmann, T. Helbig, F. Schindler, N. Salgo, M. Brzezińska, M. Greiter, T. Kiessling, D. Wolf, A. Vollhardt, A. Kabaši, C. H. Lee, A. Bilušić, R. Thomale, and T. Neupert. Reciprocal skin effect and its realization in a topoelectrical circuit. *Phys. Rev. Res.*, 2(2):023265, 2020.
- [37] T. Helbig, T. Hofmann, S. Imhof, M. Abdelghany, T. Kiessling, L. W. Molenkamp, C. H. Lee, A. Szameit, M. Greiter, and R. Thomale. Generalized bulk–boundary correspondence in non-hermitian topoelectrical circuits. *Nat. Phys.*, 16(7):747–750, 2020.

- [38] K. Xu, X. Zhang, K. Luo, R. Yu, D. Li, and H. Zhang. Coexistence of topological edge states and skin effects in the non-hermitian su-schrieffer-heeger model with long-range nonreciprocal hopping in topoelectric realizations. *Phys. Rev. B*, 103(12):125411, 2021.
- [39] D. Zou, T. Chen, W. He, J. Bao, C. H. Lee, H. Sun, and X. Zhang. Observation of hybrid higher-order skin-topological effect in non-hermitian topoelectrical circuits. *Nat. Commun.*, 12(1):7201, 2021.
- [40] J. C. Budich and E. J. Bergholtz. Non-hermitian topological sensors. *Phys. Rev. Lett.*, 125(18):180403, 2020.
- [41] F. Koch and J. C. Budich. Quantum non-hermitian topological sensors. *Phys. Rev. Res.*, 4(1):013113, 2022.
- [42] H. Yuan, W. Zhang, Z. Zhou, W. Wang, N. Pan, Y. Feng, H. Sun, and X. Zhang. Non-hermitian topoelectrical circuit sensor with high sensitivity. *Adv. Sci.*, 10(9):e2301128, 2023.
- [43] H. T. Teo, S. Mandal, Y. Long, H. Xue, and B. Zhang. Pseudomagnetic suppression of non-hermitian skin effect. *Sci. Bull.*, 69(11):1667–1673, 2024.
- [44] G. G. Liu, S. Mandal, P. Zhou, X. Xi, R. Banerjee, Y. H. Hu, and B. Zhang. Localization of chiral edge states by the non-hermitian skin effect. *Phys. Rev. Lett.*, 132(11):113802, 2024.
- [45] N. Hatano and D. R. Nelson. Localization transitions in non-hermitian quantum mechanics. *Phys. Rev. Lett.*, 77:570, 1996.
- [46] M. Ezawa. Non-hermitian boundary and interface states in nonreciprocal higher-order topological metals and electrical circuits. *Phys. Rev. B*, 99(12):121411, 2019.
- [47] B. Liu, Y. Li, B. Yang, X. Shen, Y. Yang, Z. H. Hang, and M. Ezawa. Experimental observation of non-hermitian higher-order skin interface states in topological electric circuits. *Phys. Rev. Res.*, 5:043034, 2023.
- [48] S. Yao and Z. Wang. Edge states and topological invariants of non-hermitian systems. *Phys. Rev. Lett.*, 121:086803, 2018.
- [49] K. Xu, X. Zhang, K. Luo, R. Yu, D. Li, and H. Zhang. Coexistence of topological edge states and skin effects in the non-hermitian su-schrieffer-heeger model with long-range nonreciprocal hopping in topoelectric realizations. *Phys. Rev. B*, 103:125411, 2021.
- [50] K. Bai, L. Fang, T.-R. Liu, J.-Z. Li, D. Wan, and M. Xiao. Nonlinearity-enabled higher-order exceptional singularities with ultra-enhanced signal-to-noise ratio. *Natl. Sci. Rev.*, 10(7):nwac259, 2023.
- [51] T. Chen, D. Zou, Z. Zhou, R. Wang, Y. Feng, H. Sun, and X. Zhang. Ultra-sensitivity in reconstructed exceptional systems. *Natl. Sci. Rev.*, 11(12):nwae278, 2024.
- [52] W. Deng et al. Ultrasensitive integrated circuit sensors based on high-order non-hermitian topological physics. *Adv. Sci.*, 10:eadp6905, 2024.
- [53] Q. Wang, Z. Fu, L. Ye, H. He, W. Deng, J. Lu, and Z. Liu. Non-hermitian acoustic möbius insulator. *Phys. Rev. B*, 111(10):L100101, 2025.